

A COMPUTATION-BASED ANALYSIS OF PHOTON-INDUCED FISSION*

D. Mosher[†], J.W. Schumer, J.P. Apruzese[†], R.J. Commisso, D.D. Hinshelwood, S.L. Jackson, D.P. Murphy, and S.B. Swanekamp

*Plasma Physics Division, Naval Research Laboratory
4555 Overlook Ave. SW, Washington, DC 20375 USA*

Abstract

A single burst of radiation created by 100-ns pulsed power can be used to induce photofission in fissionable material. In NRL experiments, the 8-MV Mercury bremsstrahlung spectrum irradiates a depleted-uranium plate several meters from the diode, and the resulting delayed-fission neutrons are measured. In this work, the LSP particle-in-cell code is used to model electron flow in the vacuum feed and diode, and the ITS Monte-Carlo codes are used to extract the x-ray spectrum from the diode and transport it to the DU plate. The delayed-fission-neutron yield is determined from the known dependence of the fission cross-section on photon energy. In this calculational chain, the only free parameter is the fraction of ions flowing in the diode, which affects the orbits of electrons impacting the bremsstrahlung converter. The ion fraction therefore determines the radial and angular distributions of x-rays emitted by the converter, which in turn, determine the DU neutron yield, the radial x-ray distribution emitted by the anode, and the angular distribution of x-ray dose. These three experimental measurements are compared to the modeling to determine the ion fraction that gives the best agreement between the measurements and computations: about 0.4% for the experiments discussed here.

I. INTRODUCTION

Intense Pulsed Active Detection (IPAD) [1] uses a single burst of probing radiation created by 100-ns pulsed power to induce photofission in fissionable material, the products of which can be measured. In one such series of NRL experiments, the 8-MV, 200-kA, 50-ns Mercury [2] bremsstrahlung spectrum irradiated a depleted-uranium (DU) plate 5 m from the x-ray converter, and delayed-fission neutrons were recorded by ³He detectors at various distances from the plate. [3]

In this work, the LSP particle-in-cell (PIC) code [4] is used to model electron flow in the vacuum feed and diode produced by the full Mercury voltage pulse, and the ITS set of Monte-Carlo codes [5] are used to extract the x-ray

spectrum from the diode and transport it to the DU plate. The delayed-fission-neutron yield is determined from the fission cross-section. In this calculational chain, the only free parameter is the fraction of ions flowing in the diode [6], which affect the electron orbits in the LSP computations that determine the radial and angular distributions of electrons impacting the bremsstrahlung-converter package. The ion fraction therefore determines the radial and angular distributions of x-rays emitted by the converter, which, in turn, determine the DU neutron yield, the radial x-ray distribution emitted by the anode, and the angular distribution of x-ray dose. These three experimental measurements are compared to the modeling to determine the ion fraction which best agrees with the three experimental measurements. Good agreement between the modeling and Mercury experiments provides confidence that this calculational approach can be used to predict future experimental performance.

Assumptions made in this first-principles modeling of delayed-neutron yield from the DU plate are supported by MCNPX Monte-Carlo computations [7] that use chain-model x-ray spectra as input. MCNPX provides the delayed-neutron spectra, including neutrons scattered from the Mercury cell environment, that are incident on the experimental array of ³He detectors. [8] The chain-model neutron yields are compared to the measured ³He count rates using other MCNPX computations for the detector sensitivity versus incident neutron energy [9].

The analysis presented here refers to a series of 8-MV Mercury shots conducted during the first half of 2010 that employed a 23-cm diode gap separating an 8.42-cm-radius hemispherical cathode from a 19.8-cm-radius planar anode. The anode converter package consisted of a 17- μ m-thick Al foil in front of a 152- μ m-thick Ta converter [2], backed by a 1.9-cm-thick Al beam stop. X-rays exiting the converter package towards the DU plate were attenuated by a 2-cm-thick Al Mercury endplate. The 30-cm-square, 2.5-cm-thick DU plate was located 5 m from the converter on the machine axis and inclined at 45 degrees to it. For this configuration, roughly 10^8 photo-fissions were induced in the DU. Ongoing research employing larger AK gaps, a collimator to reduce off-axis x-ray dose, and prompt-fission-neutron measurements are discussed in a companion paper. [2]

*Worked supported by the Office of Naval Research and the Defense Threat Reduction Agency.

DISTRIBUTION STATEMENT A. Approved for public release; distribution is unlimited.

[†]Independent contractor to NRL through L3 Communications, Chantilly, VA 20151 email: dave.mosher.ctr@nrl.navy.mil

II. LSP COMPUTATIONS

A series of LSP PIC simulations were performed to model the electron distribution incident on the anode converter and Mercury chamber walls throughout the Mercury voltage pulse. These simulations for the diode region were electrically-driven by a forward-going waveform from a representative full-system LSP simulation of an open-circuit load driven by forward-going waves from experimental current and voltages at the upstream pulse-forming-line [10, 11]. The diode-region simulations self-consistently modeled both power-flow electrons born in the magnetically-insulated inductive voltage adder and electrons emitted by the cathode. The 1.3-m long, 51.4-ohm constant-impedance coaxial line has dimensions of 39.68-cm diam (anode) and 16.84-cm diam (cathode). A hemispherical cathode terminated the inner line of the coax. After the cathode electric field exceeded 200 kV/cm, electrons were emitted in a space-charge-limited (SCL) fashion. Figure 1 compares the measured and LSP-computed electrical characteristics at the diode. The experimental voltage is calculated from the Mendel transmission-line algorithm. [12] The excellent agreement demonstrates that the LSP simulations can provide realistic electron distributions.

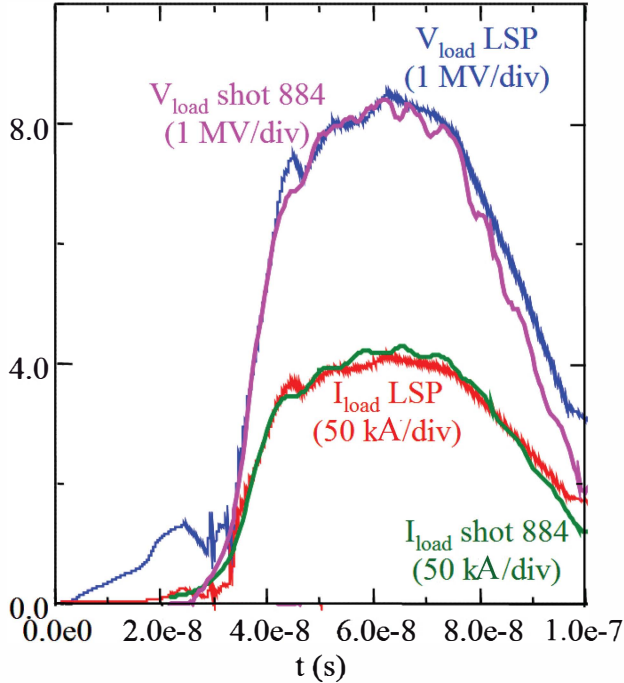


Figure 1. Comparison of measured and LSP-computed load electrical characteristics.

Electron scattering and energy loss in the bremsstrahlung converter were modeled self-consistently by LSP. Excessive electron-beam heating can form plasma on the anode surface, permitting SCL ion emission to occur. Because strong ion emission can cause unfavorable electron pinching, the diode geometry and converter-package materials were chosen to limit the anode surface

temperature rise to roughly 400-deg C. With SCL ion emission suppressed, much lower currents of electron-impact ion emission, suggested by measurements on the Sandia National Laboratories HELIA accelerator, were included in the modeling. [6] In LSP, ion charges are created at the anode surface in a specified ratio to the incident local electron charges. This ratio, the only free parameter in our modeling, was varied between 0% and 0.6% in LSP and the calculational-chain results for each ratio were compared to the experiment.

Figure 2 compares LSP snapshots of electron flow at peak voltage (the I,V characteristics do not depend on ion fraction) for the cases of 0% and 0.6% ions. The LSP geometry described above is shown in magenta with the anode converter (A), cathode (K), and chamber-wall inner diameter labeled. As the voltage rises from zero, electrons flowing along the coax go initially to the wall.

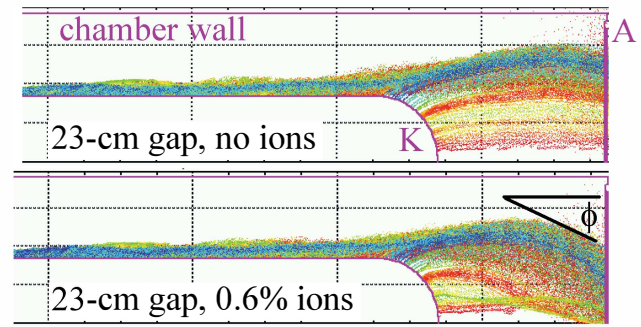


Figure 2. LSP snapshots of electron flow at peak voltage.

Electrons emitted from the hemisphere provide a rising bias current and B-field that bends flow-electron orbits gradually inward, striking the converter when high voltage is achieved. Increasing the ion fraction allows earlier lift-off from the wall, decreasing wall losses. Increasing the ion fraction also decreases the outer radius, and increases the inward angles ϕ of electrons at the converter. Figure 3 compares the average electron angle $\langle\phi\rangle$ on the converter versus radius for 0% and 0.6% ions, illustrating these points. These angles determine the angular distribution of x-rays exiting the converter.

III. ITS COMPUTATIONS

To couple LSP to ITS, LSP outputs the spatial and momentum coordinates of electron macro-particles crossing each surface of the converter package and chamber wall incrementally in time. For the work presented here, a single, time-integrated particle list is constructed for electrons striking the front surface of the converter. For each value of ion fraction, this 10^7 -particle list is input into Cyltran, the 2D r-z version of ITS, to determine the spatial and angular distribution of x-radiation exiting the Mercury chamber. A simple illustration of this process is shown in Fig. 4. Here, θ represents the viewing angle for x-rays in the far field.

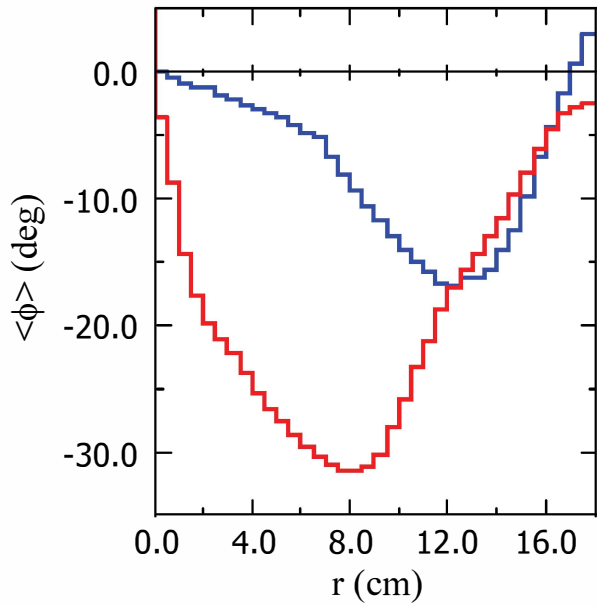


Figure 3. Average electron angle vs converter radius for 0% and 0.6% ions. Negative angles are inward.

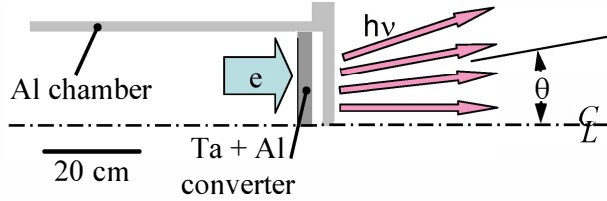


Figure 4. ITS Cyltran configuration used in the analysis.

Figure 5 shows the far-field on-axis x-ray spectra produced per electron incident on the converter for 0% and 0.6% ions. The smaller angles associated with 0% and 0.6% ions

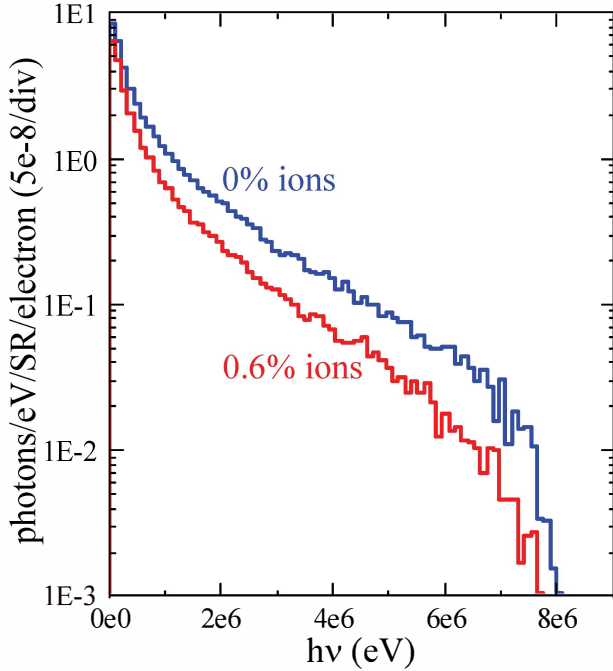


Figure 5. Far-field on-axis x-ray spectra per electron incident on the converter for 0% and 0.6% ions.

ions produce higher on-axis x-ray intensity due to relativistic beaming: nearly a factor-of-3 higher at high photon energies than 0.6% ions. Figure 6 shows the average x-ray spectral intensity vs θ in low-photon-energy (0 - 1 MeV) and high-photon-energy (6.5 - 7.5 MeV) bins for 0% and 0.6% ions. Note that the scales for the two photon-energy ranges are different to better show the dependence at large angle: on the same scale, the high-hv plots would be an additional decade lower. The low-energy bin contributes most to the x-ray dose, while the high-energy bin is responsible for most of the photo-fissions in DU. These figures indicate a higher neutron yield from the on-axis DU plate for a lower ion fraction. The variations of intensity with angle for low-hv photons indicates that lower ion fraction will also produce a higher x-ray dose at angles below 20 degrees.

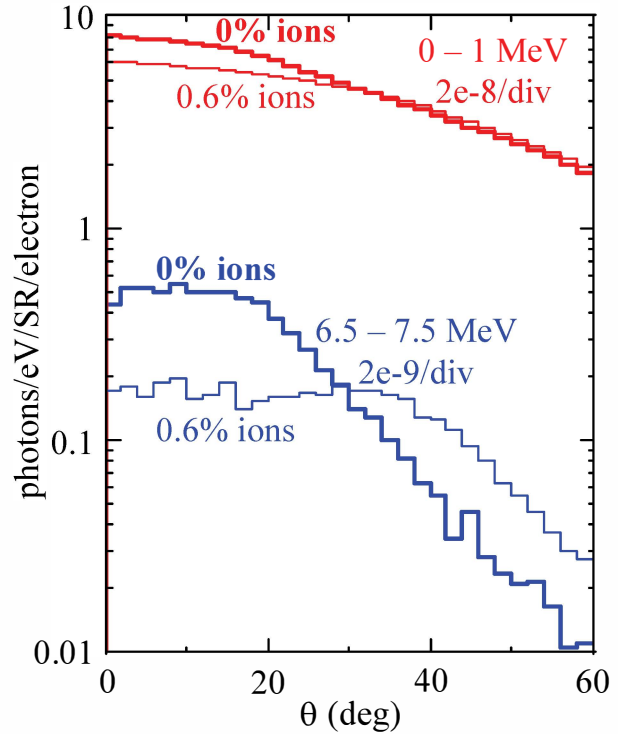


Figure 6. Average x-ray spectral intensity vs θ in low- and high-hv bins for 0% (bold) and 0.6% ions

Figure 7 compares the measured Mercury dose in CaF_2 vs angle from the machine axis with the analysis for 0% to 0.6% ion fractions. The model doses vs angle are computed from NIST x-ray absorption coefficients and the far-field Cyltran x-ray spectra in 2-degree increments. The comparison suggests that 0.2% - 0.4% ions provides the best fit to the measurements.

The pinhole camera and image plate fielded on the Mercury axis were simulated in ITS in order to compare the experimental radial image-plate (IP) profile with those modeled for different ion fractions. Full 3D ITS Accept simulations, that included the pinhole and IP geometries and compositions, used a particle list of x-ray macro-particles exiting the chamber endplate in the direction of

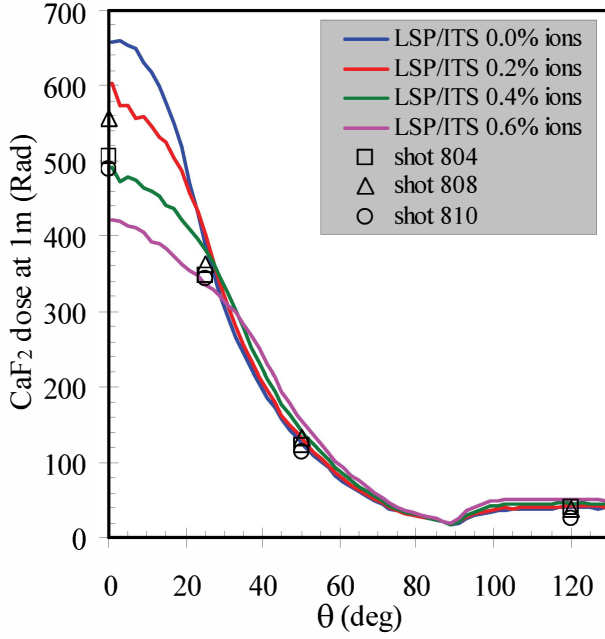


Figure 7. Comparison of measured Mercury dose vs angle with analysis for 0% to 0.6% ion fractions.

the pinhole camera to compute the radial distribution of dose in the IP. The simulated IP dose distributions are compared with experiment in Fig. 8 for various ion fractions. The IP radius has been scaled to that at the converter using the geometric pinhole magnification. Note that, as suggested by Figs. 2 and 3, increased ion fraction moves the peak radial x-ray emission to smaller radius. No single ion fraction provides a good fit to the experiment, though 0.4% places the peak emission at the correct radius. The measured emission at radii beyond that of the converter may be due to x-ray leakage through the shielding surrounding the pinhole. Also, emission from the chamber wall (from about 20- to 22-cm radius) has not been modeled. The spikes at small radii in the 0.4% and 0.5% LSP simulations have never been observed in the experiment, and constitute less than 1% of the calculated x-ray energy emitted by the converter.

IV. ANALYTIC COMPUTATIONS

Absolute-value x-ray spectra are combined with NIST x-ray absorption coefficients and published photo-fission cross-sections for DU [13] to calculate the number of fissions within the DU plate for each value of ion fraction.

$$Y_{pf} = \Omega \int N_{DU} \frac{(1 - e^{-\mu T}) S(h\nu)}{\mu(h\nu)} \sigma_{pf}(h\nu) d h\nu \quad (1)$$

In Eq. (1), Y_{pf} is the number of fissions produced in the DU plate, Ω is the plate solid angle subtending the x-ray beam, N_{DU} is the DU atomic density, $\mu(h\nu)$ is its x-ray absorption coefficient, T is the plate thickness in the axial direction, $S(h\nu)$ is the absolute on-axis ITS x-ray spectral

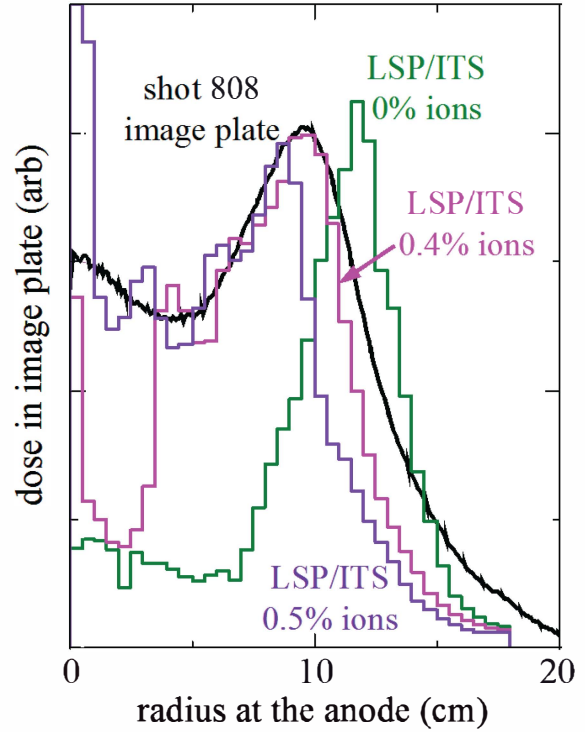


Figure 8. Comparison of simulated dose distributions in the image plate with experiment for various ion fractions.

intensity incident on the plate, and $\sigma_{pf}(h\nu)$ is the photo-fission cross-section. The absolute x-ray spectra are obtained by multiplying the spectra per electron of Fig. 5 by Q/e , where Q is the electron charge striking the front surface of the converter. Q increases slightly with increased ion fraction as losses to the chamber wall are reduced: from 11.8 mC for 0% to 13.5 mC for 0.6% ions. (About 11% of these charges are double-counted electrons which are back-scattered from the anode surface and returned to it by the diode electric field.) The delayed-neutron yield is determined from the fission yield using $4.6 \times 10^{-2} Y_{pf}$ [14]. To compare predicted neutron fluences with the measurements, the delayed-neutron yield from the DU is assumed to be emitted isotropically.

Delayed neutrons from photo-fissions were measured by an array of ^3He detectors at various distances from the DU plate. [2,3] To compare the ^3He measurements with the above analysis, MCNPX was first used to convert the number of count events in the detector to incident delayed-neutron fluence [9]. As this conversion factor depends on the incident neutron spectrum, other MCNPX computations used the ITS x-ray spectra incident on the DU to determine the neutron spectra, including the contribution of neutrons reflected from the Mercury-cell concrete walls, floor, and ceiling [8]. Figure 9 shows this delayed-neutron spectrum at 1 m from the plate in the direction of the ^3He detectors. Also shown is the detector sensitivity R as a function of neutron energy (read on right). Averaging $R(E)$ over the spectrum leads to a detector sensitivity $\langle R \rangle = 30.4$ counts/neutron/cm². The

measured counts on the ^3He detectors are divided by $\langle R \rangle$ to determine the incident delayed-neutron fluences.

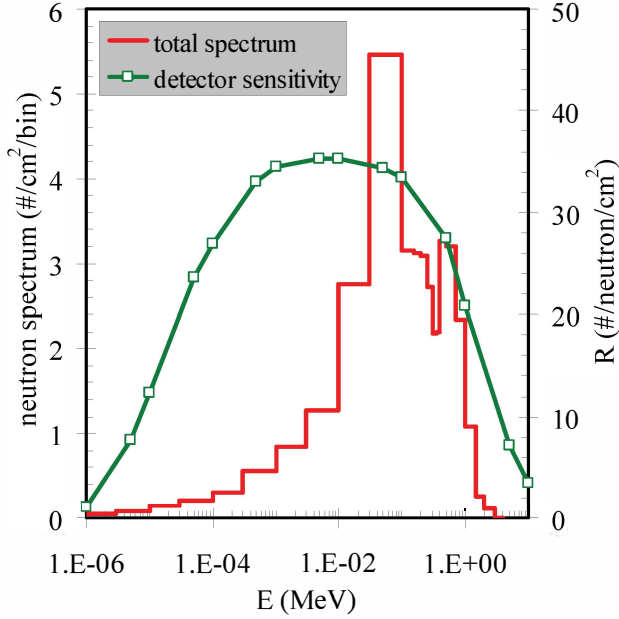


Figure 9. MCNPX neutron spectrum 1 m from the DU and reflected from the test cell environment. Also shown is the detector sensitivity R as a function of neutron energy (read on right).

The fluences on the ^3He detectors at various distances from the plate do not show the inverse-square fall-off with distance expected from the analysis because they include the room-scattered contribution [8]. In order to account for this contribution, a 4.5-neutron/cm^2 room-scatter fluence is subtracted from the calculated detector fluences. This value provides the best-fit to an inverse-square fall-off of neutron fluence to compare with the analysis. The results of this calculation are shown in Fig. 10, which plots the room-subtracted fluences on the ^3He detectors vs their distances from the DU plate for three Mercury shots. Overlaid on these data are the corresponding results of the analysis for 0% to 0.6% ion fractions. This comparison suggests that ion fractions in the range of 0.2% to 0.4% provide the best fit of the analysis to the data.

V. SUMMARY AND CONCLUSIONS

A computational chain of LSP, ITS, MCNPX, and analytic models has been benchmarked against 3 key measurements in 8-MV, 200-kA Mercury bremsstrahlung experiments to evaluate the predictive capability of the modeling. Measured and LSP-predicted diode current and voltage characteristics are in excellent agreement, demonstrating that the simulations can provide realistic electron energy distributions on the x-ray converter. The only free parameter in the computational chain is the

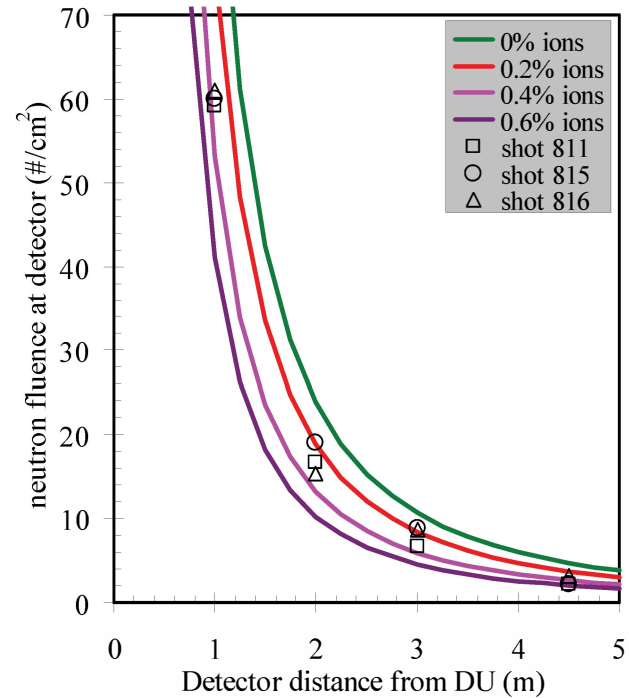


Figure 10. Room-subtracted fluence on the ^3He detectors vs distance from the DU plate compared with analysis for 0% to 0.6% ion fractions.

diode ion-charge fraction, which affects the electron radial and angular distributions impacting the x-ray converter. The three computed key comparisons with experiment that depend on this ion fraction are: the angular x-ray dose distribution, the diode radial x-ray distribution, and the computed neutron yield from the DU plate. For these comparisons, an ion fraction of 0.2% to 0.4% yields good agreement with the measurements, providing confidence that this computational-chain approach can be used to predict the performance of future IPAD experiments.

Extension of the chain modeling to recent higher-neutron-yield, 33-cm-gap experiments on Mercury [2] is ongoing. LSP computations associated with this effort have shown that varying the electron-emission threshold from the 200 kV/cm used above can have an effect similar to changing the ion fraction. Experiments designed to measure the actual ion fraction are planned to remove this ambiguity and provide better understanding of the underlying physics.

VI. REFERENCES

- [1] S.B. Swanekamp, J.P. Apruzese, R.J. Comisso, D. Mosher, and J.W. Schurer, "An Analysis of Intense Pulsed Active Detection (IPAD) for the Detection of Special Nuclear Materials," these Proceedings. In press, IEEE Trans. Nucl. Sci.

- [2] D.D. Hinshelwood, R.J. Allen, J.P. Apruzese, R.J. Commisso, G. Cooperstein, S.L. Jackson, D. Mosher, D.P. Murphy, P.F. Ottinger, J.W. Schumer, S.B. Swanekamp, B.V. Weber, and F.C. Young, "High-Power, Pulsed Bremsstrahlung Source for Inducing Photo-Fission," these Proceedings.
- [3] S.L. Jackson, R.J. Allen, J.P. Apruzese, R.J. Commisso, D.D. Hinshelwood, D. Mosher, D.P. Murphy, P.F. Ottinger, J.W. Schumer, S.B. Swanekamp, F.C. Young, G. Cooperstein, A.W. Hunt, H.A. Seipel, and M.A. Gagliardi, "Detectors for Intense, Pulsed Active Detection," Proc. IEEE Nuclear Science Symp. (Knoxville, TN, 2010), pp. 516-522.
- [4] D.V. Rose, D.R. Welch, B.V. Oliver, R.E. Clark, D.L. Johnson, J.E. Maenchen, P.R. Menge, C.L. Olson, and D.C. Rovang, "Coupled particle-in-cell and Monte Carlo transport modeling of intense radiographic sources," J. Appl. Phys. **91**, 3328–3335 (2002).
- [5] J.A. Halbleib, R.P. Kensek, G.D. Valdez, S.M. Seltzer, and M.J. Berger, "ITS: The Integrated TIGER Series of electron/photon transport codes - Version 3.0," IEEE Trans. Nucl. Sci. **41**, 1025–1030 (1992).
- [6] T.W.L. Sanford, J.A. Halbleib, J.W. Poukey, A.L. Pregenzer, R.C. Pate, C.E. Heath, R. Mock, G.A. Mastin, and D.C. Ghiglia, "Measurement of electron energy deposition necessary to form an anode plasma in Ta, Ti, and C for coaxial bremsstrahlung diodes," J. Appl. Phys. **66**, 10–22 (1989), and references therein.
- [7] X-5 Monte Carlo Team, "MCNP - A General Monte Carlo N-Particle Transport Code," Los Alamos National Lab. Rep. LA-UR-1987, (2005).
- [8] J.P. Apruzese, R.J. Commisso, J.W. Schumer, D. Mosher, S.B. Swanekamp, S.L. Jackson, D.D. Hinshelwood, F.C. Young, G. Cooperstein, and R.J. Allen, "Room Scattering Effects on the Measured Spatial Distribution of Delayed Photofission Neutrons from Depleted Uranium," 38th IEEE International Conf. on Plasma Sci., (Chicago, IL, June 2011).
- [9] S.B. Swanekamp, F.C. Young, S.L. Jackson, and R.J. Commisso, "Neutron Detector Designs for Detecting Fission Neutrons in Intense Pulsed Environments," NSS/MIC (Valencia, Spain, October 2011) and submitted for publication to IEEE Trans. Nucl. Sci.
- [10] J.W. Schumer, R.J. Allen, R.J. Commisso, G. Cooperstein, D.D. Hinshelwood, D.P. Murphy, S.J. Stephanakis, S.B. Swanekamp, and F.C. Young, Proc. 15th IEEE International Pulsed Power Conf., (Monterey, CA, June 2005), p. 1201.
- [11] R.J. Allen, R.J. Commisso, G. Cooperstein, P.F. Ottinger, J.W. Schumer, "Extension of the Operating Point of the Mercury IVA from 6 to 8 MV," these Proceedings.
- [12] P.F. Ottinger and J.W. Schumer, Phys. Plasmas **13**, 063109 (2006). Equation 2 therein with $g = 0.82$.
- [13] J.T. Caldwell, E.J. Dowdy, B.L. Berman, R.A. Alvarez, and P. Meyer, "Giant resonance for actinide nuclei: Photoneutron and photofission cross sections for ^{235}U , ^{236}U , ^{238}U , and ^{232}Th ," Phys. Rev. **C21**, 1215-1231 (1980).
- [14] R.W. Waldo, R.A. Karam, and R.A. Meyer, "Delayed neutron yields: Time dependent measurements and a predictive model," Phys. Rev. **C23**, 1113-1127 (1981).